Supplementary Information

A 5V-class Cobalt-free Battery Cathode with High Loading Enabled by Dry Coating

Weiliang Yao[1], Mehdi Chouchane[2], Weikang Li[3], Shuang Bai[1], Zhao Liu[4], Letian Li[4], Alexander X. Chen[3], Baharak Sayahpour[1], Ryosuke Shimizu[3], Ganesh Raghavendran[3], Marshall A. Schroeder[5], Yu-Ting Chen[1], Darren H.S. Tan[3], Bhagath Sreenarayanan[3], Crystal K. Waters[6], Allison Sichler[6], Benjamin Gould[6], Dennis J. Kountz[6], Darren J. Lipomi[3], Minghao Zhang[3,*], Ying Shirley Meng[2,3,*]

[1]*Materials Science and Engineering, University of California San Diego, La Jolla, CA 92093, USA*

[2]*Pritzker School of Molecular Engineering, University of Chicago, Chicago, IL, 60637, USA*

[3]*Department of NanoEngineering, University of California San Diego, La Jolla, CA 92093, USA*

[4]*Materials and Structural Analysis, Thermo Fisher Scientific, 5350 NE Dawson Creek Drive. Hillsboro, Oregon 97124, USA*

[5]*Battery Science Branch, Energy Science Division, Army Research Directorate, DEVCOM Army Research Laboratory, Adelphi, MD 20783, USA*

[6]*Advanced Performance Materials Chemours Discovery Hub, The Chemours Company, Newark, DE 19713, USA*

* Corresponding authors

Email address: shirleymeng@uchicago.edu, miz016@eng.ucsd.edu

Methods

Electrode preparation and electrochemical performance measurements

Dry electrode was fabricated via the following procedure. First of all, a total 3 g of $LiNi_{0.5}Mn_{1.5}O_4$ (LNMO, from Haldor Topsoe), Polytetrafluoroethylene binder (PTFE, from Chemours) and vapor-grown carbon fiber (VGCF, from Sigma Aldrich) were weighed at a mass ratio of 93 : 2 : 5. The mixture was then transferred to a mortar pestle which was heated to 100 °C, followed by a 10-minute grinding to obtain a free-standing film. The film was placed on the hotplate and flattened by a stainless-steel cylindrical die at 100 °C. To control the desired electrode thickness, the free-standing electrode was rolled to ~100 μm, ~130 μm, ~170 μm and ~260 μm on the hot plate. Later, the films were hot calendared at 100 °C on 20-μm etched Al foil (from Tob New Energy). The mass loadings of LNMO after hot calendaring will be ~22 mg/cm^2, ~28 mg/cm^2, ~42 mg/cm^2 and ~68 mg/cm^2. These mass loadings correspond to ~3 mAh/cm^2, ~4 mAh/cm^2, ~6 mAh/cm^2 and ~9.5 mAh/cm^2. The slurry-based LNMO electrode with the same mass ratio for comparison was fabricated following the procedure reported in our previous work.[1] Electrodes with 0.5-inch diameter was punched and dried in vacuum oven at 100 °C for 24 hours. CR2032 coin cells were built for both half cell and full cell. In half cells, Li metal (Tob New Energy) was used as counter electrode. Celgard 2325 was used in 3 and 4 mAh/cm^2 level half cells while glass fiber (Whatman GF/F) was used in the 6 and 9.5 mAh/cm^2 areal loading. With Celgard 2325 separator at areal loading >6 mAh/cm^2, the electrolyte will be quickly consumed by side reactions to form dead Li due to high current density (>2 mA/cm^2). Therefore, we choose to use glassfiber separator in order to contain more electrolyte during the first few cycles. In full cells, graphite electrodes provided by Ningbo Institute of Materials Technology & Engineering (NIMTE) with 95% active materials was used as counter electrode with an N/P ratio = 1.1~1.15. Dreamweaver (Soteria) was used as the separator. All cells were assembled with the same setup presented in our previous work.[1] Gen2 electrolyte (1M $LiPF_6$ in EC: EMC = 3:7 wt.%) from Gotion was used in all cells. All-fluorinated electrolyte 1M $LiPF_6$ in FEC: FEMC = 3:7 wt.% in full cell testing and 1M $LiPF_6$ in FEC:FEMC:HFE (2:6:2 wt%) in 6.0 mAh/cm^2 dry-LNMO half cell cycling were provided by U.S. Army Research Laboratory (ARL). 50 μL electrolyte was added in 3.0

and 4.0 mAh/cm^2 level loading. Since the area of LNMO electrode is ~1.267 cm^2, electrolyte to capacity ratios in 3.0 and 4.0 mAh/cm^2 level loading are ~14 g/Ah and ~11 g/Ah respectively. For 6.0 and 9.5 mAh/cm^2 level loading, glassfiber separator was used so electrolyte is in large excess amount. In full cell cycling protocols, 1 C is defined as 147 mA/g with a voltage range from 3.3 V to 4.85 V. C/10 was performed as formation in first two cycles, followed by C/3 for 300 and 1000 cycles. All the electrochemical testing were carried out at room temperature using the Neware Battery Test System (Neware China). EIS measurements were conducted with a BioLogic VSP-300. An applied AC potential of 10 mV over a frequency range from 1 MHz to 1 mHz was used. Linear sweep voltammetry (LSV) measurements were also conducted with BioLogic VSP-300 with a sweeping rate of 1 mV/s from open circuit voltage to 5.5 V. Cyclic voltammetry testing was performed using Arbin (Arbin Instruments). The sweeping rate was set as 1 mV/s from 3 V to 5 V.

Binder selection process

Selection of an appropriate PTFE for this specific application is critical. Choosing a PTFE having a melt creep viscosity of at least about 1 x 10^{11} poise at 380 ^{o}C is essential.[2-3] PTFE is a polymer comprised of repeating units of tetrafluoroethylene (TFE) monomer. With such a high melt creep viscosity of at least 1 x 10^{11} poise it is neither melt-processible nor does it readily dissolve in any common solvents unlike PVDF binder. Melt creep viscosity is an indirect measure of molecular weight. PTFE of high melt creep viscosity exhibits fibrillation when shear stress is applied to the PTFE particles especially above the beta transition temperature of PTFE where a well-ordered triclinic structure transforms to a partially ordered hexagonal crystalline phase at a temperature of 19 ^{o}C or less depending on comonomer content. PTFE molecular chains fold in an accordion pattern in submicron crystallites when PTFE powder is formed. Teflon^{TM} PTFE used in this work was developed by the Chemours Company (Wilmington, DE) to maximize the fibril formation character as well as the blending capability with the VGCF fibers in order to form an intimate PTFE/VGCF fibrous structure that maximizes both electrical conductivity and porosity in the resulting electrode structure.

Materials characterizations

LSV/CV: In **Figure S1A**, when carbon is absent in the working electrodes, the specific current obtained along sweeping is relatively low compared to carbon-containing working electrode. The peak observed at 4.2 V for the Al foil electrode represents the self-passivation behavior of aluminum.[4] With the presence of carbon, the specific oxidation current rapidly increases at a potential above 4.2 V, showing the continuous decomposition of carbonate-based electrolyte triggered by carbon. Fastest passivation in CV (**Figure S1B**) is achieved in vapor grown carbon fibers (VGCF) due to its lower specific surface area (**Table S2**) and less reactive sites. The cathodic peaks at 3.9 V and 4.2 V in the VGCF working electrode can be attributed to the PF_6^- de-intercalation peaks from VGCF since it is a partially graphitized carbon.[5] The decreased intensity of both peaks from the second to the third cycle shows this intercalation reaction is reversible and will be passivated along cycling.

SEM and PFIB-SEM-EDS: FEI Apreo® scanning electron microscope (SEM) was used to capture the electrode cross-sections with different areal loadings. A 5 kV accelerating voltage and 0.1 nA beam current were set throughout the testing. Thermo Scientific Helios 5 Hydra Plasma Focused Ion Beam (PFIB) DualBeam was used for large-area cross-section milling and the subsequent SEM imaging. Xe^+ ion source was used to mill and then clean the cross-section of various electrode samples. Rough milling was performed at a FIB acceleration voltage of 30 keV, 2.5 μA to generate a 300-350 μm wide cross-section through the entire thickness of the electrode. The rough milled cross-sections were then polished with automatic rocking mill technology to reduce curtaining effect and other polishing artifact at a beam current of 200 nA. High resolution imaging was carried out using the SEM column from the DualBeam instrument. Energy Dispersive Spectroscopy (EDS) elemental analysis is carried out with an Oxford Instrument Ultim Max detector

XPS and HRTEM: All cycled full cells were disassembled in the glovebox (MBraun) to prevent air exposure. X-ray photoelectron spectroscopy (XPS) was performed using a Kratos AXIS Supra. All the cycled electrodes were prepared without washing, and the transfer process was air-tight to avoid any possible degradation. The XPS was operated

using an Al anode source at 15 kV with a 10^{-8} Torr vacuum level. All XPS measurements were collected using an auto neutralizer during acquisition. Survey scans were collected with a 1.0 eV step size, followed by high-resolution scans with a step size of 0.1 eV. All the data were calibrated using a C 1s peak at 284.6 eV. High resolution transmission electron microscopy (HRTEM) results for pristine and cycled samples were obtained on ThermoFisher Talos X200 equipped with a Ceta camera operated at 200 kV. To prepare TEM samples, powder samples were dispersed on a lacey carbon grid inside the Ar glovebox. The loading and transferring grids to TEM were carefully executed to prevent air exposure.

ICP-MS: The Ni/Mn amounts on the cycled graphite electrodes from the coin cell were confirmed by Inductively coupled plasma mass spectrometry (ICP-MS, iCAP RQ, Thermo Fisher Scientific). Cycled graphite electrodes from cells stopped at 50^{th} and 100^{th} cycle were punched as 1/8-inch laminates and then soaked in a 3 mol/L H_2SO_4 solution overnight for a fair comparison. Then the supernatant was collected and further diluted for ICP check.

Capillary XRD: The samples were prepared by sealing the powders in boron-rich glass capillary tubes (Charles Supper Company, 0.7mm diameter) inside an Ar-filled glovebox with < 0.1 ppm H_2O level. The X-Ray Diffraction (XRD) measurements were done using a Bruker APEX II Ultra diffractometer with Mo Kα (λ= 0.71073 Å) radiations at 50 kV and 50 mA to check the crystal structures. The diffraction images gathered by the 2D detector within an angular range of 4° to 40° were merged and integrated with DIFFRAC.EVA (Bruker, 2021) to produce 2d-plots.

Physical adsorption of nitrogen at the liquid nitrogen temperature: Micromeritics™ ASAP 2020 gas adsorption/surface area measurement apparatus was used for BET analysis of the different carbon particles. The carbon sample (VGCF, SC65 and KB) to be analyzed was loaded into the round bottom sample tubes and was weighed. Sample tubes were covered with heat jacket and degassing was done to the sample to remove any volatile compounds. Vacuum setpoint was set at 100 µmHg and temperature was held at 250 ^{o}C for degassing, for 5 hours. After degassing, the sample tubes stripped of heating jacket was lowered into a dewar flask filled with liquid nitrogen. The adsorption cycle was performed with nitrogen gas as the adsorbate. The relative pressure (P/Po) was measured at equilibration interval of

90 seconds. The adsorption isotherms and the pore area are obtained from ASAP 2020 software once the cycle completes.

Modeling workflow

To capture the impact of the carbon additives morphology, a smaller scale was chosen compared to the one from **Figure S2**, as it can be seen from **Figure 3**. While the full thickness of the electrode is not considered, it allows to demonstrate the influence of the morphology of the electronic conductive phase on the efficiency of the electronic percolating network. To confirm that the two PFIB-SEM images can be compared, **Figure S13A** and **S13B** report the segmented PFIB-SEM images, with the phase percentages of each phase for respectively the dry-LNMO and slurry-based LNMO in **Figure S13C** and **S13D**. The two cross-sections have roughly the same amount of carbon binder domain (21.05% for the dry-LNMO versus 20.56% for the slurry-based LNMO) but the dry-LNMO has a lower amount of porosity (14.51%) compared to the slurry-based LNMO (19.15%). Since in LIB, the two limiting factors can either be the electronic or the ionic transports,[6] the lower amount of porosity could lead to an unfair comparison because of the introduction of a higher ionic transport limitation. However, as illustrated in **Figure S14**, the ionic transport is not the limiting phenomenon during the discharge since the concentration of Li^+ in the electrolyte at the end of discharge is almost uniform in both cases. Then, we can attribute the differences that will be observed in the two cases solely to the electronic transport.

Starting from a segmented 2D PFIB image, the latter would be stacked to form a thin 3D image which would then be meshed using the tool INNOV, which is freely available online, with ca. 1 million tetrahedral elements. The mesh file was exported in NASTRAN format and imported into COMSOL Multiphysics ® where the 4-D (3D spatial + 1D time) model reported in **Table S4** and **Table S5** was applied.

Mechanical testing

Measurement of Electrode Debonding Behavior using 90° Peel Tests: Dry and slurry-based electrodes were fabricated as previously decribed on top of Al current collectors. These electrode stacks were cut into similar rectangular dimensions (approx. 30 mm × 75 mm),

with the electrode covering approximately one-third of the current collector (approx. 25.4 mm × 25.4 mm). Prior to testing, the thickness of each electrode was measured using a micrometer. Adhesive tape (Scotch Magic Tape, w = 19.05 mm) was carefully placed on top of each electrode to maximize contact area and reduce possible air bubbles. A large glass cover (~2.5 kg) was placed on top of all peel test samples, followed by two Aluminum blocks (~1.2 kg each) in order to ensure constant and uniform pressure on top of each sample. Peel test samples were left in this configuration overnight and tested the following day. To conduct a 90° peel test, a Mark-10 linear actuator was operated in the upright position with appropriate peel test accessories (ESM303, G1109). The current collector of each peel test sample was fixed to the sliding stage using transparent double-sided tape (3M). The adhesive tape was held by 3D-printed grips attached to the force gauge. Electrodes were delaminated in a standard 90° peel test format at a rate of 330 mm min^{-1} (ASTM D3330 standards). The force was measured relative to displacement (travel) using a 10 N force gauge. After each peel test, the thickness of the electrode removed by the tape was measured using a micrometer. To process the data, the peel force was normalized by dividing the measured load by the width of the tape (w = 19.05 mm). The steady-state force required to induce failure of each electrode was calculated by averaging the force in a 15-mm travel on the force-displacement plot.

Tensile Measurements of Dry Electrodes: Dry electrodes were fabricated as previously described into rectangular strips (approx. 50 mm × 75 mm). A dogbone-shaped stencil was 3D printed (Formlabs Form 3) in order to cut the dry electrodes into the dogbone shapes (with the center rectangular dimensions measuring w = 0.6 cm and l = 1.2 cm). Prior to testing, the thickness of each dogbone was measured using a micrometer (t = 90–240 μm). The two wider edges of each dogbone-shaped electrode was wrapped with electrical tape to ensure that fracture occurred within the center rectangular region (**Figure S11**). These dogbone samples were loaded onto a linear actuator (ESM303, Mark-10) using 3D-printed grips attached to a 10 N force gauge and elongated at a rate of 1 mm min^{-1} until fracture. The resulting force-elongation data was converted to stress-strain data using the dimensions of each dogbone with a purpose-written script in Matlab 2021b. Engineering strain was calculated by dividing the elongation of the dogbone by the initial length. The

engineering stress was calculated by dividing the measured force by the initial cross-sectional area of the dogbone.

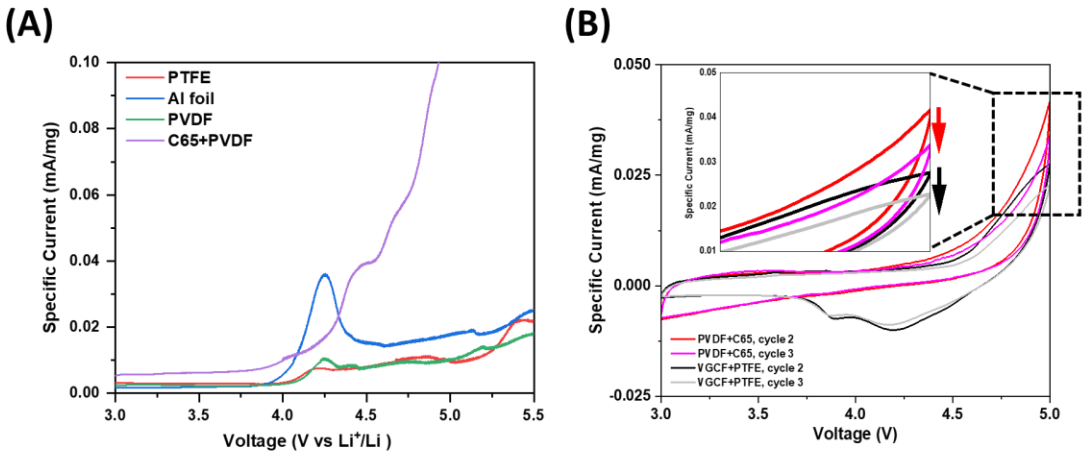

Figure S1. Oxidation Stabilities of different cell components. (**A**) Linear sweep voltammetry of PTFE, PVDF and Al current collector compared with PVDF mixed with super C65 carbon. (**B**) Passivation behavior between super C65 carbon and vapor grown carbon fiber.

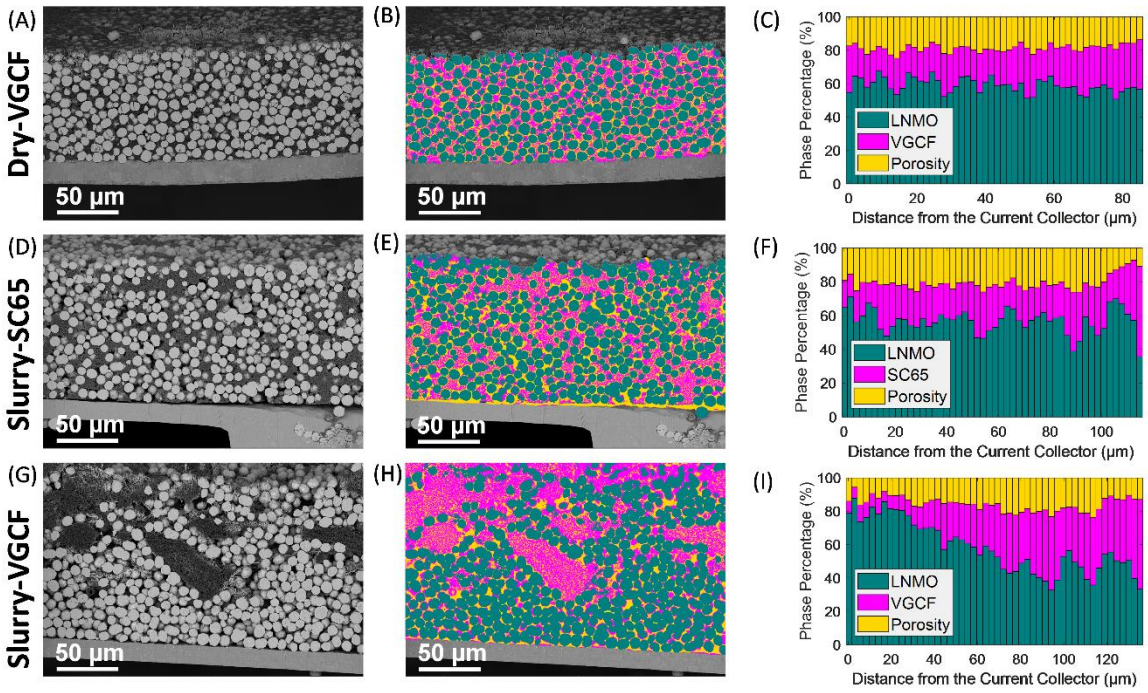

Figure S2. Visualizing of phase distribution in LNMO 3 mAh/cm^2 electrodes. PFIB cross-section of (**A**) dry-LNMO, and (**D**) Slurry-based LNMO using Super C65 carbon and (**G**) Slurry-based LNMO using VGCF. Corresponding color segmentation and phase quantification of (**B**) and (**C**) dry-LNMO; (**E**) and (**F**) Slurry-based LNMO using Super C65 carbon; (**H**) and (**I**) Slurry-based LNMO using VGCF.

These cross sections revealed that the slurry-based LNMO using VGCF exhibits severe carbon agglomeration, indicating the conventional slurry mixing failed to disperse the carbon fibers as uniformly as the SC65. Consequently, in slurry-based electrodes, most of LNMO particles are not connected by VGCF, which severely hinders the electron flow from active materials to the current collector. In addition, the PTFE binder is prone to ion beam damage, so the carbon phase is identified as VGCF rather than fibrillated binder.

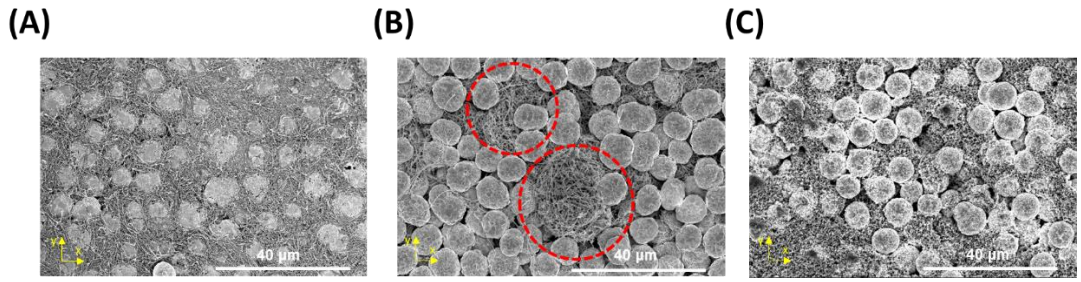

Figure S3. Top surface of electrodes: (A) dry-coated, (B), slurry-based with VGCF, and (C) slurry-based with super C65.

Similar observations were also found on the top surface of these electrodes, indicating that the VGCF powder tends to aggregate into a group of fibers.

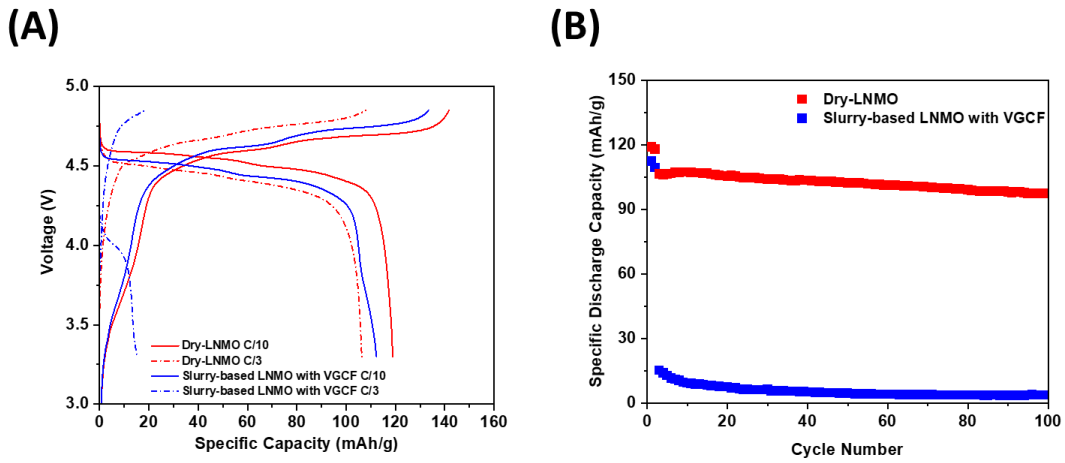

Figure S4. Electrochemical performance comparison between dry-LNMO and slurry-based LNMO electrode using VGCF in full cells. (**A**) Voltage profiles and (**B**) Cycling performance.

The lack of connection between the cathode particles and carbon fibers in slurry-based LNMO will unsurprisingly lead to extremely poor electronic percolation network and rapid impedance growth at higher C-rate, therefore contributing to drastic capacity decay.

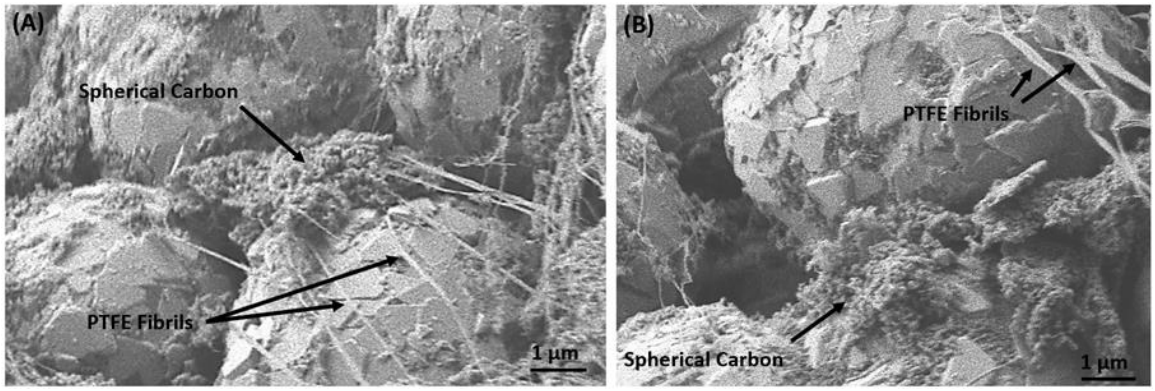

Figure S5. SEM images showing the morphology of a dry electrode using SC65 carbon. The PTFE appears as classical fibrils and the SC65 forms a conductive pathway wherever the PTFE and SC65 intersect. It can be observed that the main electronic conducting pathway is the SC65 carbon connecting several LNMO particles in a small region.

Interestingly, due to its nano-agglomerate morphology, the SC65 carbon in the dry electrode is unable to construct an effective electronic percolation network compared to VGCF, which has a similar fiber morphology as the fibrillated PTFE binder.

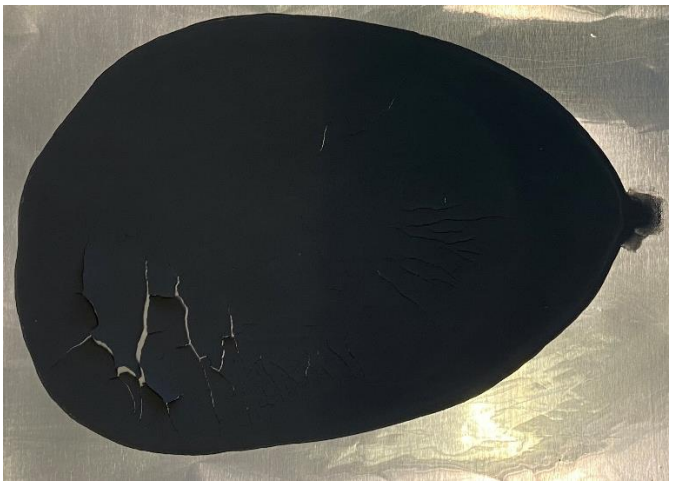

Figure S6. 6 mAh/cm^2 level slurry-based LNMO after drying process.

The drying process of a thick cathode may lead to migration of binder and carbon to the top surface of electrode due to convective and capillary force developed in the process. As a result, poor adhesion between the electrode and current collector occurs, leading to severe electrode cracking.

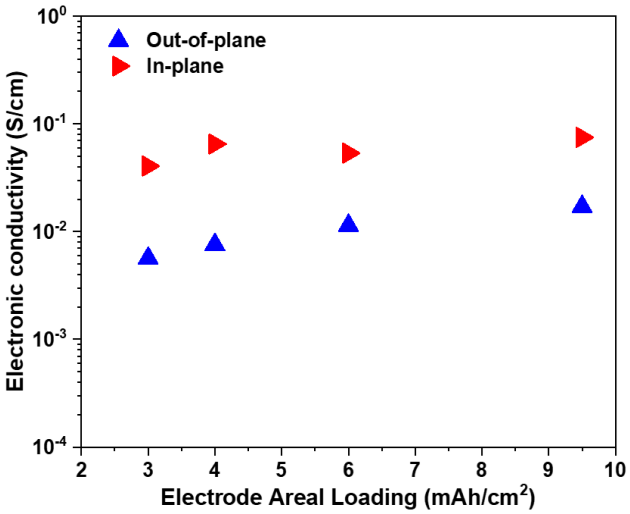

Figure S7. Electronic conductivity of dry-LNMO at various loadings: in-plane and out-of-plane conductivity at different areal loadings.

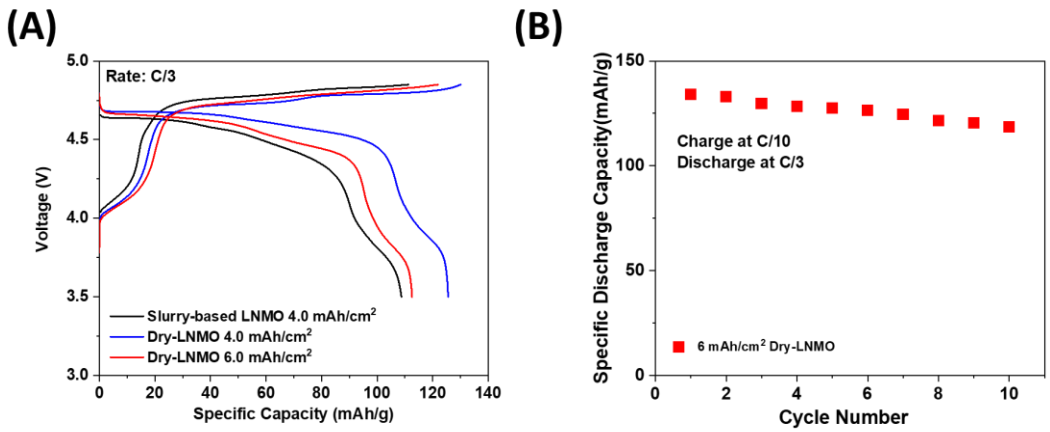

Figure S8. (A) Electrochemical performance comparison between dry-LNMO and slurry-LNMO half cells at the C/3 rate. (B) Cycling performance of 6.0 mAh/cm^2 dry-LNMO in half cell.

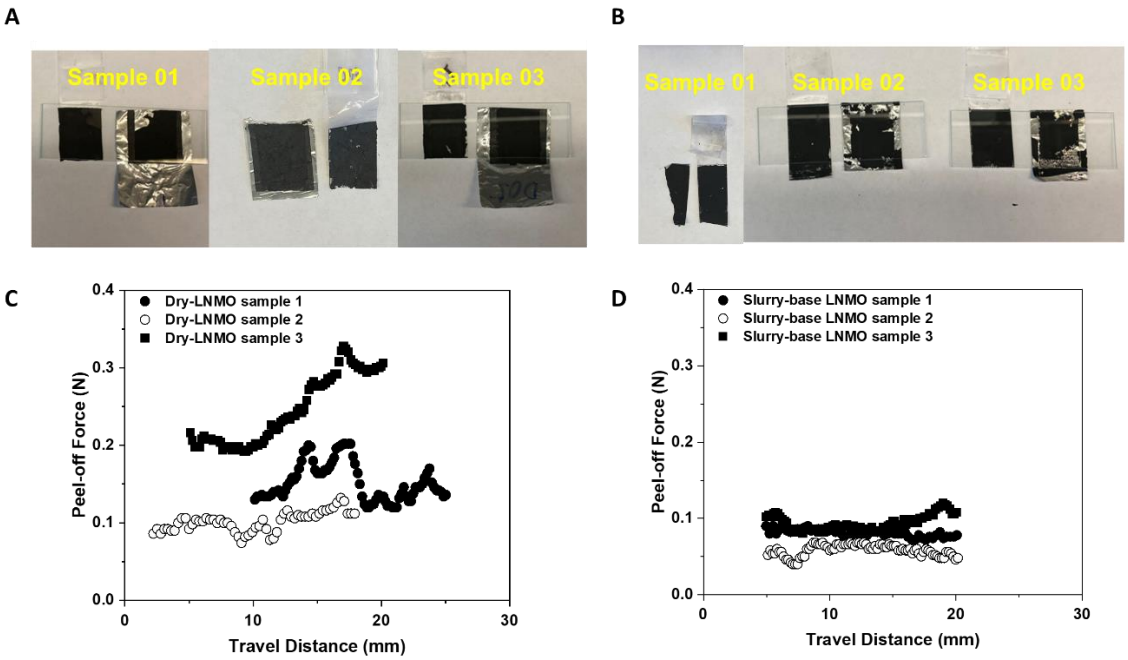

Figure S9. (**A**) dry-LNMO and (**B**) Slurry-based LNMO after peel-off testing. Change of peel-off forces along traveling of (**C**) dry-LNMO and (**D**) Slurry-based LNMO.

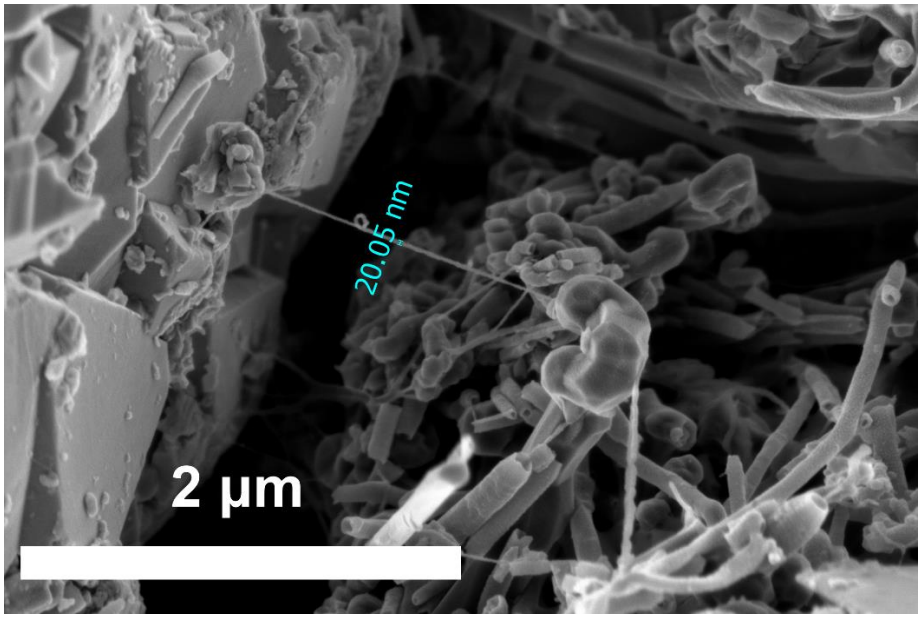

Figure S10. PFIB-SEM cross-section of dry-LNMO showing the thickness of PTFE binder after fibrillation.

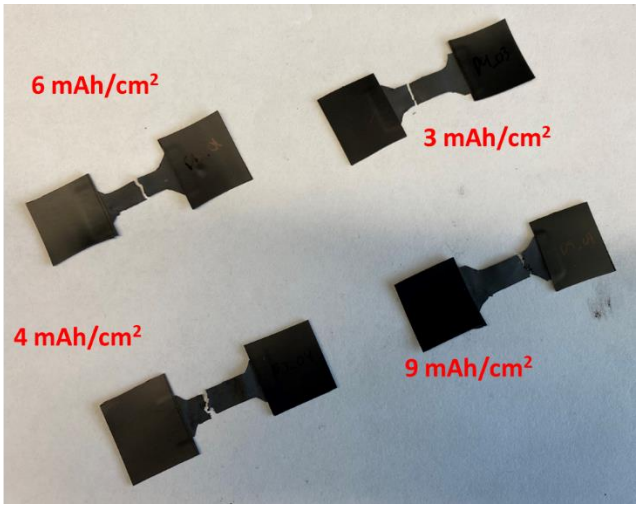

Figure S11. Representative dry-LNMO samples after tensile testing.

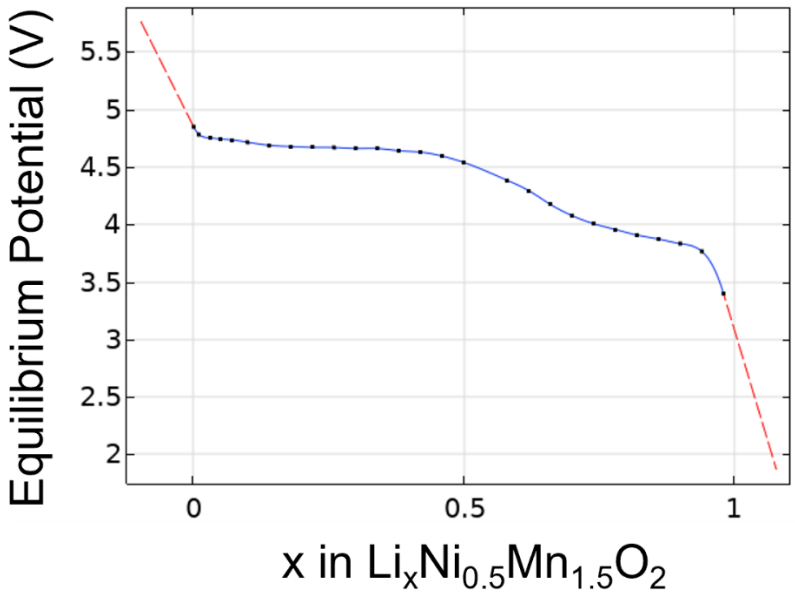

Figure S12. Equilibrium potential of Li in LNMO as a function of the state of lithiation. Fitted from [7].

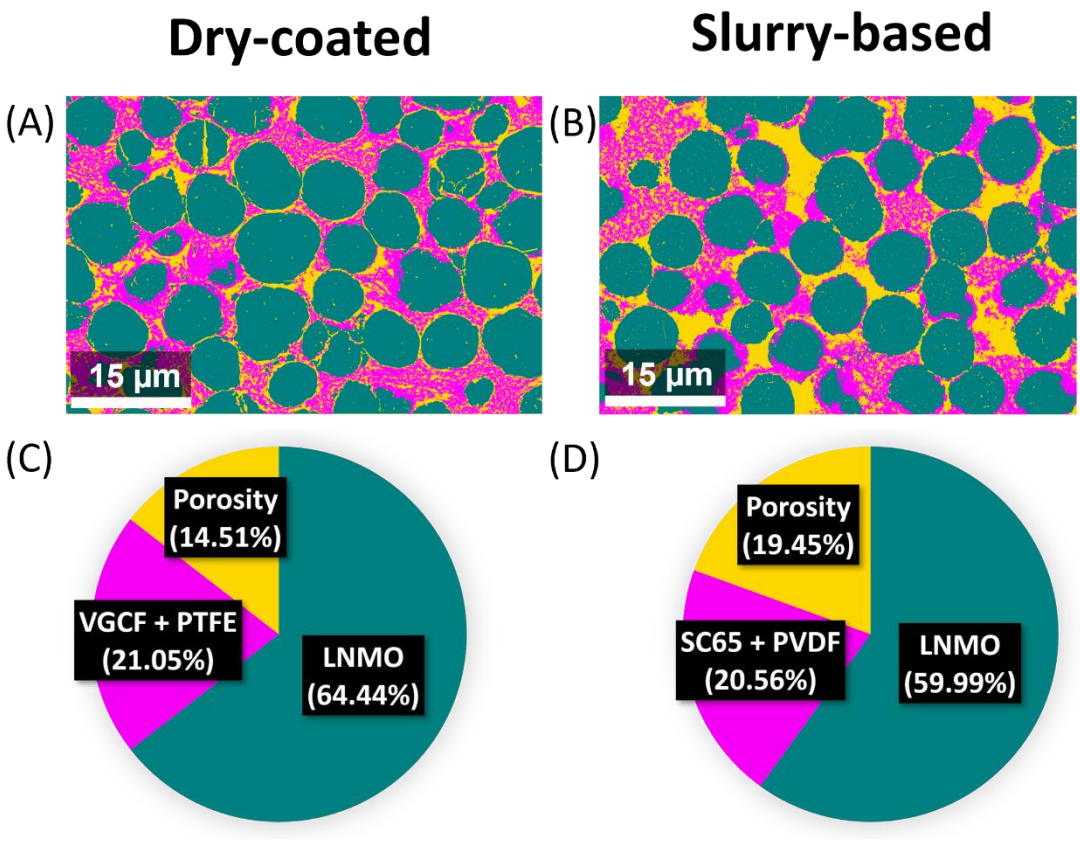

Figure S13. Segmented PFIB-SEM images of the (A) dry-coated and (B) slurry-based electrodes and their respective phase percentages with (C) the dry-LNMO with VGCF, and (D) the slurry-based LNMO with SC65. The LNMO is represented in green, the carbon and binder in pink and the porosity in yellow.

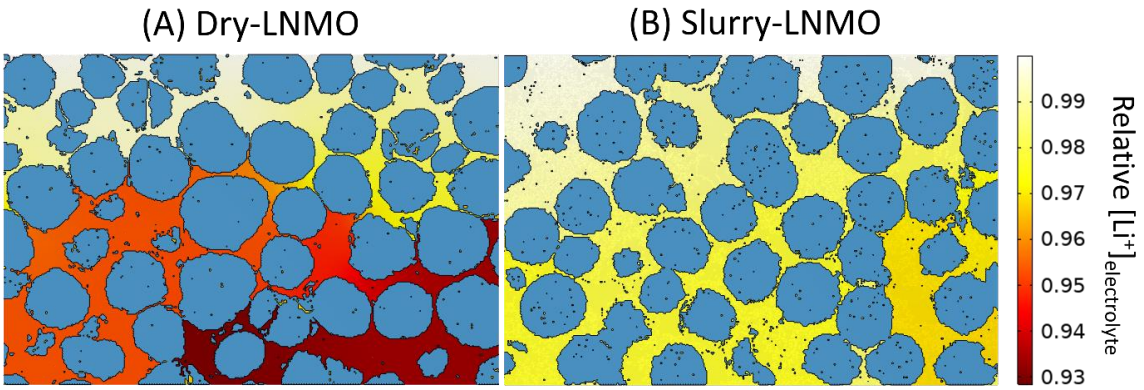

Figure S14. Distribution of the Li^+ concentration in the electrolyte at the end of discharge for (A) the dry-LNMO and (B) the slurry-LNMO with SC65.

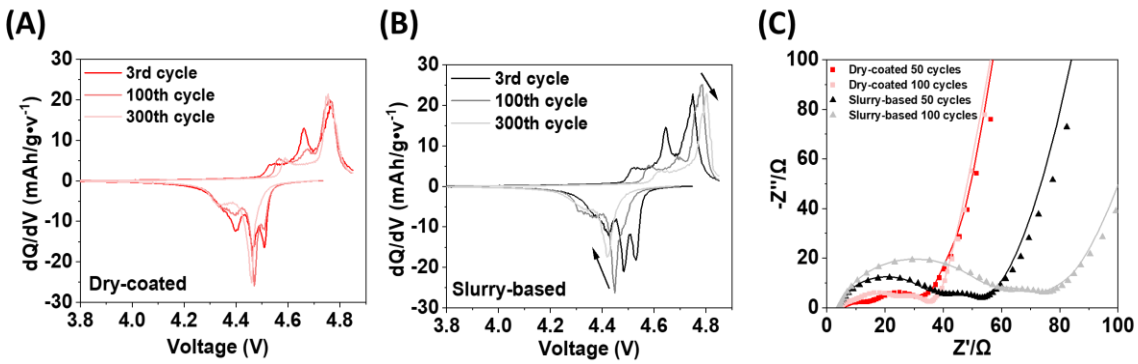

Figure S15. (A) dry-coated and (**B**) slurry-based LNMO in full cells. (**C**) The Nyquist plots of dry-LNMO and slurry-based LNMO full cells after different number of cycles.

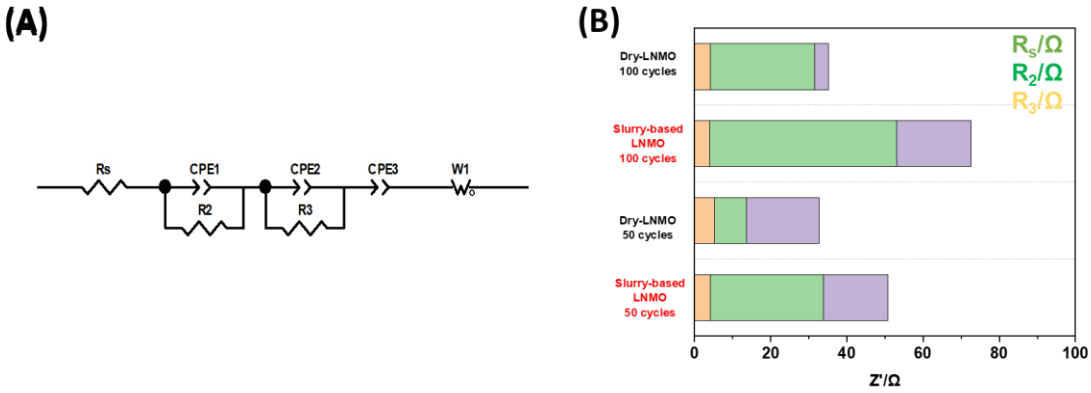

Figure S16. EIS fitting and quantification. (**A**) Equivalent circuit used for fitting. (**B**) Resistance values from different circuit components in the fitting.

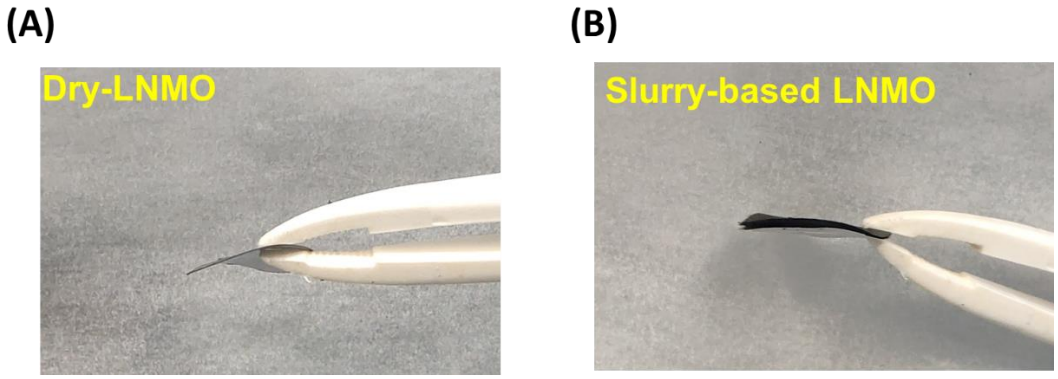

Figure S17. Adhesion check between electrode and current collector after 300 cycles. Side view of cycled (**A**) dry-LNMO and (**B**) slurry-based LNMO.

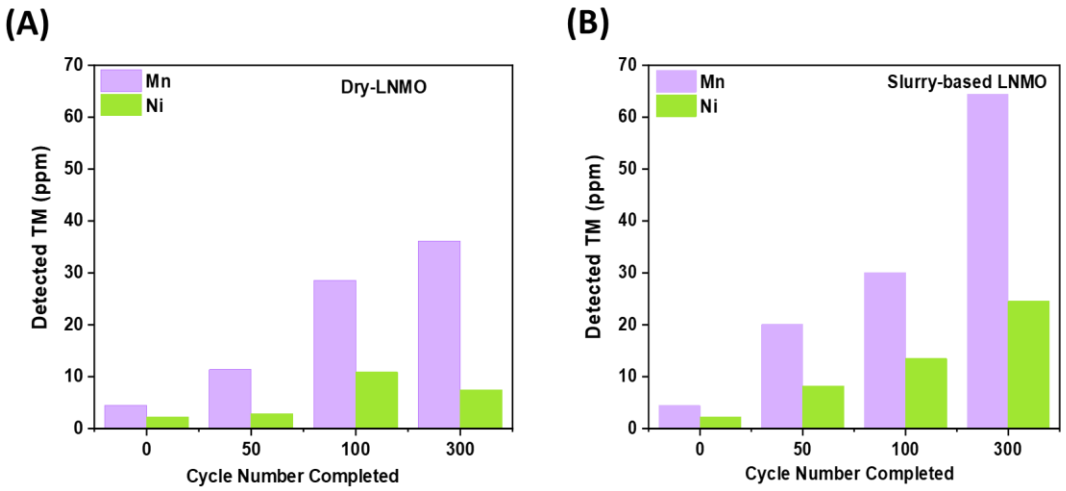

Figure S18. ICP results from cycled graphite electrodes at different cycle numbers. (**A**) Dry-LNMO. (**B**) Slurry-based LNMO.

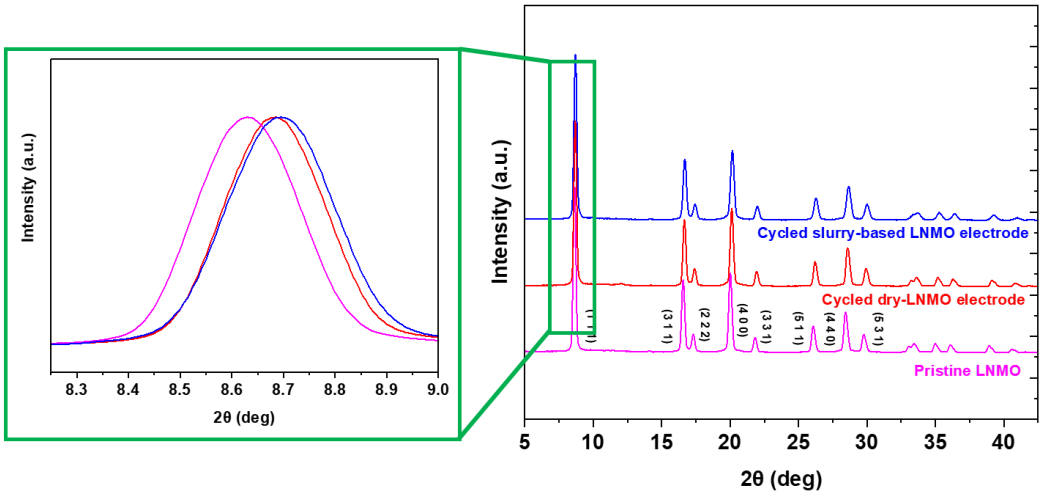

Figure S19. XRD results of cycled LNMO using both slurry-based and dry electrode methods.

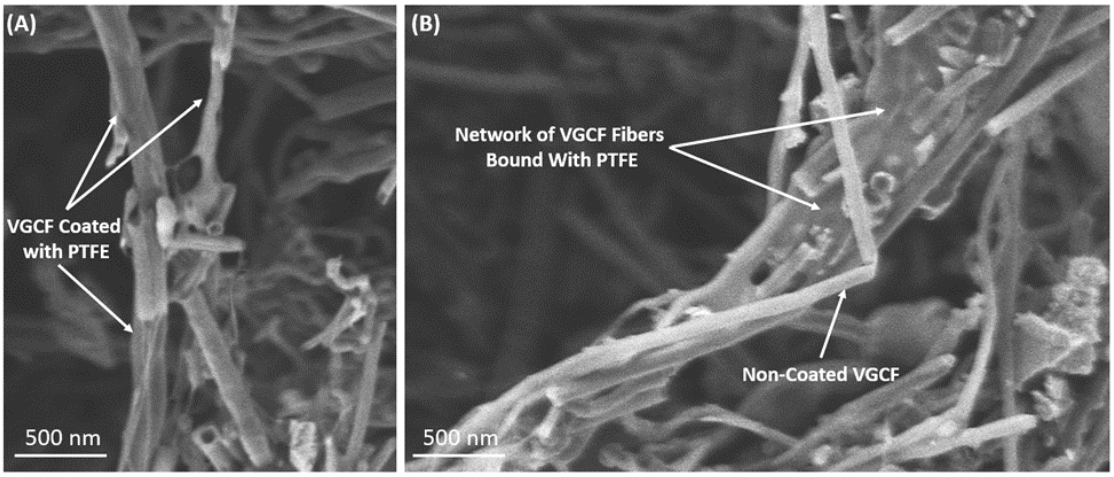

Figure S20. SEM images showing the unique interactions between PTFE and VGCF in the dry electrode. The PTFE forms a pseudo-coating on the outside of the VGCF fibers further reducing side reactions. Moreover, the PTFE and VGCF seem to align resulting in a combined electronically conducting, supportive web within the electrode.

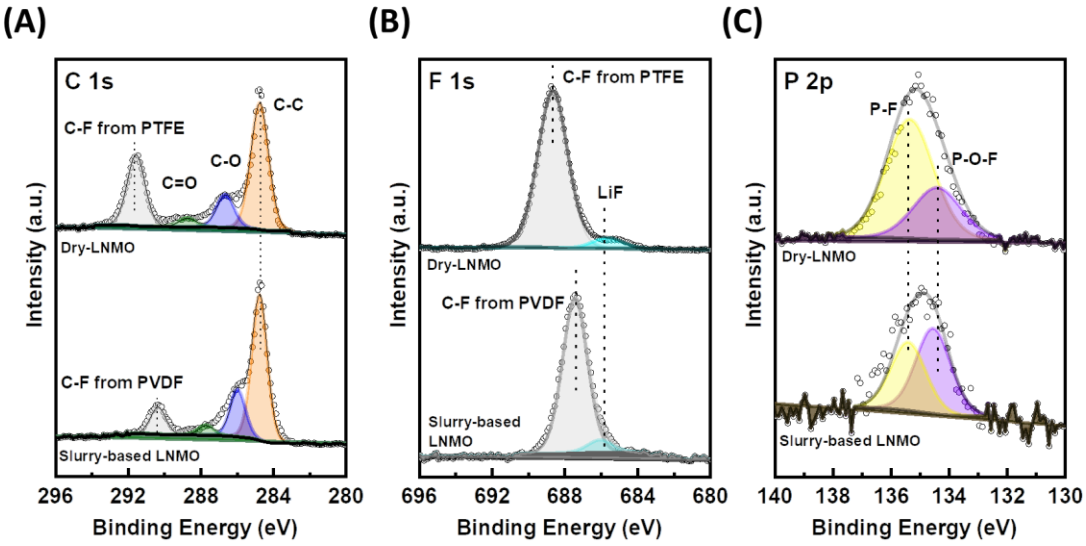

Figure S21. XPS spectra of (**A**) C 1s, (**B**) F 1s and (**C**) P 2p of the cycled dry-LNMO and slurry-based LNMO.

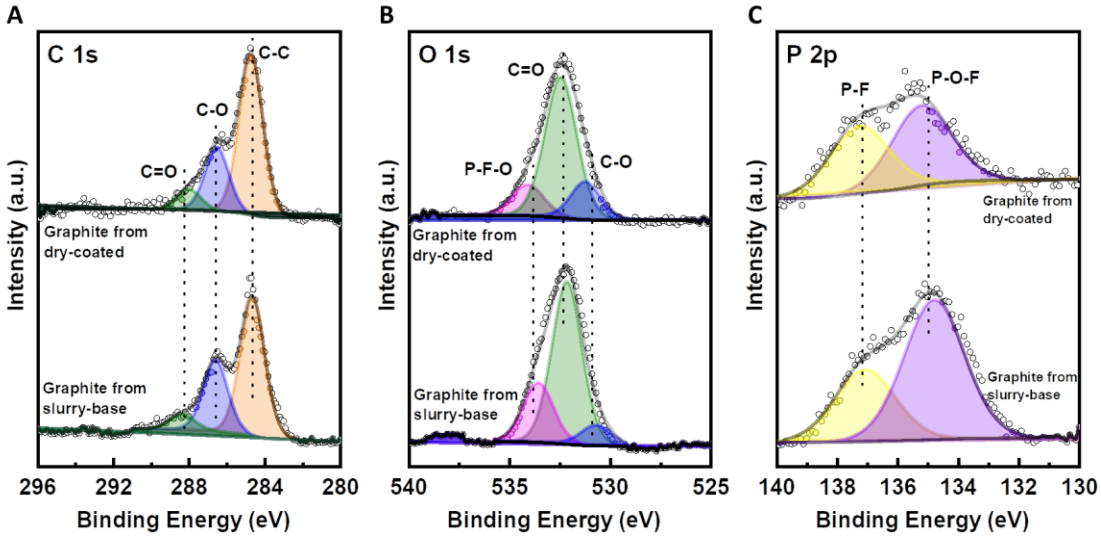

Figure S22. XPS spectra of (**A**) C 1s, (**B**) O 1s and (**C**) P 2p of the cycled graphite from dry-LNMO and slurry-based LNMO full cells.

Table S1. Energy density estimation in a lithium-ion battery's single-layer pouch cell.

Energy density estimation in LIBs single-layer pouch cell		
Assumptions:		
Pouch Type Cell, **package and tab mass excluded**		
Model: Anode | Liq electrolyte | cathode		
Number of layers	1	1 or 1 side, 2 for 2 side
Battery Composition / kWh		
Nominal Voltage (working voltage)	4.7	V
Capacity	0.1743	Ah
Utilisation Rate	1	Frac
Areal Capacity per side	3	mAh/cm2
Total area	29.05	cm2
NP Ratio	1.15	Frac
Liquid Electrolyte Ratio	2	g/Ah
Liquid Electrolyte Density	1.3	g/cm3
Total Electrolyte required	0.3486	g
Total Electrolyte required	0.3486	g
Separator Mass	1.386	mg/cm2
Total Separator Mass	0.0402633	g
Cathode		
Cathode Active Ratio	0.93	Frac
Cathode Disc Cap	140	mAh/g
Total Cathode req	1.245	g
Al thickness	0.0016	cm
Al Density	2.7	g/cm3
Total Al CC Required	0.125496	g
Binder+Carbon Ratio	0.07	Frac
Total Binder and Carbon req	0.09370967742	g
Anode		
AnodeActive Ratio	0.95	Frac
Adnoe Disc Cap	372	mAh/g
Total Anode Required	0.5388306452	g
Cu thickness	0.0009	cm
Cu Density	8.96	g/cm3
Total Cu CC Required	0.2342592	g
Binder /Carbon Ratio	0.25	Frac
Total Binder and Carbon req	0.1417975382	g
Total Mass	0.002767956361	kg
Energy Density at Cell level	**295.962036**	**Wh/kg**

Table S2. BET results of different types of carbon additive.

Sample	Spec. Area m^2/g
Vapor-grown Carbon Fiber	18.6
Super C65	57.5
Ketjen Black	1299.2

Table S3. Stress and strain results summary from tensile testing of dry-LNMO electrodes at various areal loadings.

Tensile testing samples	Tensile strength (MPa)	Fracture strain (mm/mm)	Average values
3 mAh/cm^2 01	0.36	0.23	0.28 MPa ± 0.07 0.26 mm/mm ± 0.03
3 mAh/cm^2 02	0.24	0.27	
3 mAh/cm^2 03	0.24	0.28	
4 mAh/cm^2 01	0.26	0.19	0.25 MPa ± 0.01 0.18 mm/mm ± 0.02
4 mAh/cm^2 02	0.25	0.16	
4 mAh/cm^2 03	0.24	0.19	
6 mAh/cm^2 01	0.29	0.14	0.30 MPa ± 0.02 0.20 mm/mm ± 0.08
6 mAh/cm^2 02	0.29	0.17	
6 mAh/cm^2 03	0.32	0.29	
9.5 mAh/cm^2 01	0.25	0.25	0.25 MPa ± 0.02 0.21 mm/mm ± 0.04
9.5 mAh/cm^2 02	0.23	0.18	
9.5 mAh/cm^2 03	0.27	0.20	

Table S4. 4D-resolved electrochemical model equations.	
Lithium foil electrode	
Lithium foil current	$J_{Li} = Fk_{0,Li}\left(\frac{C_e}{C_0}\right)^{\alpha_a}\left[exp\left(\frac{\alpha_a \eta F}{RT}\right) - exp\left(\frac{-\alpha_c \eta F}{RT}\right)\right]$
Electrolyte-lithium foil boundary conditions	$D_e^{eff}\nabla C_e = \frac{J_{Li}t_+}{F}$ $\phi_e = 0$
Active material	
Material balance	$\frac{\partial C_s}{\partial t} = -\nabla(-D_{AM}\nabla C_s)$
Lithium insertion equation	$J_{AM} = i_0\left[exp\left(\frac{\beta_a \eta F}{RT}\right) - exp\left(\frac{-\beta_c \eta F}{RT}\right)\right]$ $i_0 = coeff_i \times Fk_{0,LNMO}\left(\frac{C_e}{C_0}\right)^{\beta_a} C_s^{\beta_c}(C_{s,max} - C_s)^{\beta_a}$ $coeff_{AM/Electrolyte} = 1\ ;\ coeff_{AM/CBD} = \varepsilon_{CBD}$ $\eta = \phi_{AM} - \phi_e - U$
Particle-electrolyte boundary conditions	$D_{AM}\left.\frac{\partial C_s}{\partial r}\right\|_{r=R_i} = \frac{J_{AM}t_+}{F}$
Charge balance	$\nabla \cdot (\sigma_{AM}\nabla\phi_{AM}) = 0$
Particle-current collector boundary condition	$\lvert J_{CC}\rvert = \sigma_{AM}\nabla\phi_{AM}$
Overpotential	$\eta = \phi_{AM} - \phi_e - U$
Electrolyte	
Material Balance	$\frac{\partial(\varepsilon_i C_e)}{\partial t} = \nabla\left(D_{e,i}^{eff}\nabla C_e + \frac{t_+ J_e}{F}\right)$ $D_{e,i}^{eff} = D_e\varepsilon_i^{p_i}$; i = separator, electrolyte, CBD
Charge Balance	$\nabla \cdot J_e = 0$ $J_e = -\sigma_{e,i}^{eff}\nabla\phi_e - k_{De}\nabla \ln\ C_e$ $k_{De} = \frac{2RT\sigma_{e,i}^{eff}}{F}(1 - t_+)$ $\sigma_{e,i}^{eff} = \sigma_e\varepsilon_i^{p_i}$; i = separator, electrolyte
Electrolyte-current collector boundary conditions	$D_{e,i}^{eff}\nabla C_e$=0 $\nabla\phi_e = 0$
Carbon-binder domain	
Charge balance	$\nabla \cdot \left(-\sigma_{CBD}^{eff}\nabla\phi_{CBD}\right) = 0$

Table S5. 4D-resolved electrochemical model parameters.		
Name	Symbol	Value/Definition
Anodic charge transfer coefficient of NMC	α_a	0.5
Cathodic charge transfer coefficient of Li foil	α_c	0.5
Anodic charge transfer coefficient of NMC	β_a	0.5
Cathodic charge transfer coefficient of Li foil	β_c	0.5
Porosity of the CBD	ε_{CBD}	0.5
Porosity of the separator	ε_{sep}	0.6
Over potential	η (V)	Φ_{AM}- Φ_E-U
Electronic conductivity of AM[8]	σ_{AM}	1×10^{-4} S.m^{-1}
Electronic conductivity of CBD[9, 10]	σ_{CBD}	700 S.m^{-1}
Ionic conductivity of the electrolyte (fitted from[9])	σ_e (S.m^{-1})	$1.98055\times10^{-3}\times C_e\times\exp(-8.148\times10^{-4}\times(C_e/C_0)^{1.3094}) + 8.374\times10^{-2}$
Density of AM[12]	ρ_{AM}	4.381×10^{6} g. m^{-3}
AM potential	Φ_{AM} (V)	
CBD potential	Φ_{CBD} (V)	
Electrolyte potential	Φ_e (V)	
Standard concentration in the electrolyte	C_0	1000 mol.m^{-3}
Li^+ concentration	C_e (mol.m^{-3})	
Initial Li^+ concentration in the electrolyte	$C_{e,moy}$	1000 mol.m^{-3}
Li concentration in the AM	C_s (mol.m^{-3})	
Maximal Li concentration in AM[12]	$C_{s,max}$	23864 mol.m^{-3}
Theoretical Capacity of AM[12]	Cap_{Th} (mAh/g)	146
Capacity	Cap (Ah)	$Cap_{Th}\times\rho_{AM}\times V_{AM}$
Diffusion coefficient of Li^+ in the electrolyte (fitted from [11])	D_e(m^2.s^{-1})	$-1.665\times10^{-13}\times C_e + 5.293\times10^{-10}$
Li diffusion coefficient in AM[13]	D_{AM}	6.43×10^{-15} m^2.s^{-1}
Faraday constant	F	96485 C.mol^{-1}
Current density pulse value at the current collector	J_{CC} (A.m^{-2})	Cap×Crate/ SCC
Li Foil kinetic constant	$k_{0,Li}$	1×10^{-3} mol.m^{-2}.s^{-1}

LNMO kinetic constant	$k_{0,LNMO}$	1×10^{-11} mol.m^{-2}.s^{-1}
Bruggeman exponent coefficient for the electrolyte	$p_{electrolyte}$	0
Bruggeman exponent coefficient for the separator	p_{sep}	1.5
Ideal gas constant	R	8.314 J.mol^{-1}.K^{-1}
Surface area of solid in contact with the current collector	S_{CC} (m^2)	
Reference temperature	T_{ref}	298 K
Li transference number	t_+	0.363
Equilibrium Potential of LNMO (fitted from [10])	U	See below **Fig. S8**
Volume of AM	V_{AM} (m^3)	

Table S6. LNMO-Graphite full cell literature work comparison using baseline setting.

Cycle (No.)	Retention after cycles (%)	Cathode loading ($mg \cdot cm^{-2}$)	Rate ($1C=147mA \cdot g^{-1}$)	Ref
1000	**60**	**22**	**0.333**	**This work**
300	**80**	**22**	**0.333**	**This work**
175	33	21.7	0.2	[14]
100	10	21.3	1	[15]
200	~50	19.7	1	[16]
190	73	15.9	0.2	[17]
445	66	~15	0.5	[18]
100	~72	14.7	0.5	[19]
150	60.9	14.7	0.5	[20]
100	~20	12.5	0.333	[21]
255	80	~14.9	1	[22]
400	62	10	1	[23]
150	32.9	6.5	0.5	[24]
170	41	6.5	0.1	[25]

Table S7. LNMO-Graphite full cell literature review using novel modifications.

Cycle (No.)	Retention after cycles (%)	Cathode loading ($mg \cdot cm^{-2}$)	Rate ($1C=147mA \cdot g^{-1}$)	Novelty	Ref
1000	**68**	**20**	**0.333**	**Dry electrode with fluorinated electrolyte**	**This work**
1000	**60**	**22**	**0.333**	**Dry electrode with baseline electrolyte**	**This work**
280	75	21.7	0.2	Lithiated LNMO Interlayer	[14]
100	70	21.3	1	Polyvinylidene fluoride macroporous membrane	[15]
200	57	19.7	1	Addition of partially fluorinated ether and FEC	[16]
190	79	15.9	0.2	LiBFEP electrolyte additive	[17]
820	80	~14.9	1	LiDFOB electrolyte additive	[22]
445	82	~15	0.5	Use of low-surface area LNMO	[18]
1000	69	14.7	0.5	Sulfone-base electrolyte	[20]
100	~84	14.7	0.333	Lithium malonatoborate salts as additives	[19]
100	~100	12.5	0.333	Fluorinated electrolyte with extra lithium source	[21]
400	83	10	1	Water-base CMC binder	[23]
150	76.9	6.5	0.5	Titanium doping with lithiated graphite	[24]
170	71	6.5	0.1	Crown Ether Functionalized Conductive Carbon	[25]
1000	80	5	1	Guar gum (GG) binder	[26]

Table S8. Literature review of LNMO performance under elevated temperature.

Cycle (No.)	Retention after cycles (%)	Cathode loading ($mg \cdot cm^{-2}$)	Rate ($1C=147mA \cdot g^{-1}$)	Ref
100	**70**	**22**	**0.333**	**This work**
90	54.5	14	0.5	[20]
100	66.7	12.5	0.333	[27]
50	71.4	10.6	0.2	[28]
40	88	9.3	0.5	[29]
20	70	8	0.1	[30]

REFERENCES

1. Li, Weikang, et al. "Enabling high areal capacity for Co-free high voltage spinel materials in next-generation Li-ion batteries." *Journal of Power Sources* 473 (2020): 228579.
2. US3819594 "Tetrafluoroethylene fine powder resin of a copolymer of tetrafluoroethylene and perfluoro(alkyl vinyl ether)"
3. Sina Ebnesajjad, Fluoroplastics Vol. 1 Non-Melt Processible Fluoropolymers and Expanded PTFE Applications Hand Bauer, Werner, *et al*. "Influence of dry mixing and distribution of conductive additives in cathodes for lithium ion batteries." *Journal of Power Sources* 288 (2015): 359-367.
4. Hirata, K., Kawase, T., & Sumida, Y. (2020). Passivation Behavior of Aluminum in a Carbonate-Free Electrolyte Based on Lithium Bis (fluorosulfonyl) imide and Sulfolane. *Journal of The Electrochemical Society*, 167(14), 140534.
5. Qi, Xin, *et al*. "Investigation of PF6− and TFSI− anion intercalation into graphitized carbon blacks and its influence on high voltage lithium ion batteries." *Physical Chemistry Chemical Physics* 16.46 (2014): 25306-25313.
6. Mistry, Aashutosh N., Kandler Smith, and Partha P. Mukherjee. "Secondary-phase stochastics in lithium-ion battery electrodes." *ACS applied materials & interfaces* 10.7 (2018): 6317-6326
7. Rahim, A. S. A.; Kufian, M. Z.; Arof, A. K. M.; Osman, Z. Variation of Li Diffusion Coefficient during Delithiation of Spinel LiNi0.5Mn1.5O4. *J. Electrochem. Sci. Technol* **2022**, *13* (1), 128–137.
8. Jung, S. H.; Kim, D. H.; Brüner, P.; Lee, H.; Hah, H. J.; Kim, S. K.; Jung, Y. S. Extremely Conductive RuO2-Coated LiNi0.5Mn1.5O4 for Lithium-Ion Batteries. *Electrochimica Acta* **2017**, *232*, 236–243.
9. Chen, C.-F.; Verma, A.; Mukherjee, P. P. Probing the Role of Electrode Microstructure in the Lithium-Ion Battery Thermal Behavior. *J. Electrochem. Soc.* **2017**, *164* (11), E3146–E3158.
10. Chen, Y.-H.; Wang, C.-W.; Zhang, X.; Sastry, A. M. Porous Cathode Optimization for Lithium Cells: Ionic and Electronic Conductivity, Capacity, and Selection of Materials. *Journal of Power Sources* **2010**, *195* (9), 2851–2862.
11. Nyman, A.; Behm, M.; Lindbergh, G. Electrochemical Characterisation and Modelling of the Mass Transport Phenomena in LiPF6–EC–EMC Electrolyte. *Electrochimica Acta* **2008**, *53* (22), 6356–6365.
12. Xie, Y.; Srinivasan, V.; Kaiya, H.; Takahashi, K. Particle-Scale Path-Dependent Behavior of LixNi0.5Mn1.5O4 Electrode in Li-Ion Batteries: Part I. Experimental Study. *J. Electrochem. Soc.* **2019**, *166* (12), A2513.
13. Liu, W.; Shi, Q.; Qu, Q.; Gao, T.; Zhu, G.; Shao, J.; Zheng, H. Improved Li-Ion Diffusion and Stability of a $LiNi_{0.5}Mn_{1.5}O_4$ Cathode through in Situ Co-Doping with Dual-Metal Cations and Incorporation of a Superionic Conductor. *J. Mater. Chem. A* **2017**, *5* (1), 145–154.

14. Fan, D., Lu, D., Wu, S., Zeng, R., He, J., Shu, D., & Cai, Y. (2020). Mechanism of a lithiated interlayer for improving the cycle life of high voltage Li-ion batteries using a commercial carbonate electrolyte. *The Journal of Physical Chemistry C*, 124(15), 8057-8066.
15. Arbizzani, C., De Giorgio, F., & Mastragostino, M. (2014). Characterization tests for plug-in hybrid electric vehicle application of graphite/LiNi0. 4Mn1. 6O4 cells with two different separators and electrolytes. *Journal of Power Sources*, 266, 170-174.
16. Kim, C. K., Kim, K., Shin, K., Woo, J. J., Kim, S., Hong, S. Y., & Choi, N. S. (2017). Synergistic effect of partially fluorinated ether and fluoroethylene carbonate for high-voltage lithium-ion batteries with rapid chargeability and dischargeability. *ACS applied materials & interfaces*, *9*(50), 44161-44172.
17. Milien, M. S., Beyer, H., Beichel, W., Klose, P., Gasteiger, H. A., Lucht, B. L., & Krossing, I. (2018). Lithium bis (2, 2, 2-trifluoroethyl) phosphate Li [O2P (OCH2CF3) 2]: a high voltage additive for LNMO/graphite cells. *Journal of The Electrochemical Society*, *165*(11), A2569.
18. Michalak, B., Berkes, B. B., Sommer, H., Brezesinski, T., & Janek, J. (2017). Electrochemical cross-talk leading to gas evolution and capacity fade in LiNi0. 5Mn1. 5O4/Graphite full-cells. *The Journal of Physical Chemistry C*, *121*(1), 211-216.
19. Li, Y., Veith, G. M., Browning, K. L., Chen, J., Hensley, D. K., Paranthaman, M. P., ... & Sun, X. G. (2017). Lithium malonatoborate additives enabled stable cycling of 5 V lithium metal and lithium ion batteries. *Nano Energy*, 40, 9-19.
20. Alvarado, Judith, et al. "A carbonate-free, sulfone-based electrolyte for high-voltage Li-ion batteries." *Materials Today* 21.4 (2018): 341-353.
21. Hu, Libo, Khalil Amine, and Zhengcheng Zhang. "Fluorinated electrolytes for 5-V Li-ion chemistry: Dramatic enhancement of LiNi0. 5Mn1. 5O4/graphite cell performance by a lithium reservoir." *Electrochemistry communications* 44 (2014): 34-37.
22. Hofmann, Andreas, et al. "Additives for Cycle Life Improvement of High-Voltage LNMO-Based Li-Ion Cells." *ChemElectroChem* 6.20 (2019): 5255-5263.
23. De Giorgio, Francesca, et al. "Graphite//LiNi0. 5Mn1. 5O4 Cells Based on Environmentally Friendly Made-in-Water Electrodes." *ChemSusChem* 10.2 (2017): 379-386.
24. Höweling, Andres, et al. "Evidence of loss of active lithium in titanium-doped LiNi0. 5Mn1. 5O4/graphite cells." *Journal of Power Sources* 274 (2015): 1267-1275.
25. Saneifar, Hamidreza, Karim Zaghib, and Daniel Belanger. "Crown ether functionalized conductive carbon for high-voltage spinel LiMn1. 5Ni0. 5O4/graphite cell." *ACS Applied Energy Materials* 3.1 (2019): 647-657.
26. Kuenzel, Matthias, et al. "Co-Crosslinked Water-Soluble Biopolymers as a Binder for High-Voltage LiNi0. 5Mn1. 5O4| Graphite Lithium-Ion Full Cells." *ChemSusChem* 13.10 (2020): 2650-2660.

27. Hu, Libo, Zhengcheng Zhang, and Khalil Amine. "Fluorinated electrolytes for Li-ion battery: An FEC-based electrolyte for high voltage LiNi0. 5Mn1. 5O4/graphite couple." *Electrochemistry communications* 35 (2013): 76-79.
28. Aktekin, Burak, *et al*. "Understanding the capacity loss in LiNi0. 5Mn1. 5O4–Li4Ti5O12 lithium-ion cells at ambient and elevated temperatures." *The Journal of Physical Chemistry C* 122.21 (2018): 11234-11248.
29. Aktekin, Burak, et al. "How Mn/Ni ordering controls electrochemical performance in high-voltage spinel LiNi0. 44Mn1. 56O4 with fixed oxygen content." *ACS Applied Energy Materials* 3.6 (2020): 6001-6013.
30. Kraytsberg, Alexander, et al. "Atomic Layer Deposition of a Particularized Protective MgF2 Film on a Li‐Ion Battery LiMn1. 5Ni0. 5O4 Cathode Powder Material." *ChemNanoMat* 1.8 (2015): 577-585.